Top-of-the-line corrosion

29

Marc Singer
Ohio University, Athens, OH, United States

29.1 Review of water condensation modeling

The water condensation rate (WCR) is typically calculated by evaluating the water dropout via temperature change in a given section of pipe. However, this approach can lead to underprediction, for example in the case of cold spots, as condensation rates are averaged. A more accurate, albeit more cumbersome, approach considers local heat transfer at the top of the pipe. Both methods are presented here.

29.1.1 Water dropout approach

The most common methodology used by flow assurance software to predict WCR involves the determination of the temperature drop along a section of pipe and of the amount of water condensation from the vapor phase. A comprehensive heat loss module, considering pipeline and outside environment characteristics, is necessary to determine the temperature profile. Thermodynamic models can be used to calculate the water vapor partial pressure, which decreases along the pipe following the temperature drop. The reduction in water vapor pressure is directly used to calculate an average condensation rate considering only the upper half of the pipe area. The equation below is only valid for small sections of pipes:

$$\mathrm{WCR} = m_{\mathrm{gas}} \frac{M_{\mathrm{water}}}{M_{\mathrm{gas}}} \frac{2}{AL} \left(\frac{P_{\mathrm{vap}}^{\mathrm{in}} - P_{\mathrm{vap}}^{\mathrm{out}}}{P_{\mathrm{Total}}} \right) \tag{29.1}$$

where WCR is given in kg/m^2/s; m_{gas} is the gas mass flow rate (kg/s); M_{gas} and M_{water} are molecular weight of gas phase and water (kg/mol); $P_{\mathrm{vap}}^{\mathrm{in}}$ and $P_{\mathrm{vap}}^{\mathrm{out}}$ are vapor pressure at the inlet and outlet of the pipe section (bar); $A/2$ is half of pipe perimeter (m); and L is the pipe length of the section considered (m).

However, this method can be inaccurate in some cases because as the water vapor condenses, the bulk aqueous phase present at the bottom of the line tends to evaporate to counter the more rapid cooling of the gas phase. The water drop out does not distinguish between these two parts and only calculates an overall rate of water accumulation, i.e., the rate of water condensing from the vapor minus the rate of water evaporating from the bulk liquid. This approach can consequently underpredict the actual WCR happening locally at the top of the pipe.

Trends in Oil and Gas Corrosion Research and Technologies. http://dx.doi.org/10.1016/B978-0-08-101105-8.00029-2

29.1.2 Local water condensation approach

The calculation of local WCR is linked to the phenomenon of dropwise condensation, which has been studied extensively over the past 60 years. It can be described in terms of a four-stage scenario [1]: nucleation, growth, coalescence, and removal. The fundamentals of the mechanism and modeling of dropwise condensation have been published by Rose [2–6] over the past 30 years. As dropwise condensation is a random process, the common approach is to calculate the heat flux through a single droplet and to integrate the expression over an average distribution of drop sizes:

$$Q = \int_{r_{\min}}^{r_{\max}} q(r)N(r)dr \tag{29.2}$$

where Q is the total heat flux (W/m^2); $q(r)$ is the heat flux through an individual droplet of radius r (W/m^2); $N(r)dr$ is the number of drops per area with radius between r and $r + dr$ (m^{-2}); $r_{\max}$ and $r_{\min}$ are maximum and minimum radii of droplet (m).

Then the total heat flux includes the heat transfer due to the phase change and the presence of noncondensable gas. It has been reported that the main resistance for heat transfer comes from the presence of noncondensable gas [7–9]. The relationship between total heat flux and condensation rate can be stated in the following way [10]:

$$Q = Q_g + Q_c = h_g \times \left(T_b^g - T_i^g\right) + \mathrm{WCR} \times H_{fg} \tag{29.3}$$

where Q is the total heat flux (W/m^2); Q_g is the heat flux through the gas boundary layer (W/m^2); Q_c is the latent heat flux released by the phase change (W/m^2); h_g is the heat transfer coefficient in the gas boundary layer (W/m^2/K); $\left(T_b^g - T_i^g\right)$ is the temperature difference between bulk and vap/liq interface (K); WCR is given in kg/m^2/s; H_{fg} is the latent heat of evaporation/condensation (J/kg).

The heat transfer theory applied to dropwise condensation is well understood and has been described and applied by many authors [11–14]. The approach can be directly applied to a pipeline considering heat resistances due to the presence of noncondensable gas, the curvature of the droplet, the vapor/liquid interface, the liquid thickness and the promoter (pipe material) surface itself. The approach was described by Zhang [10] and described schematically in Fig. 29.1, assuming a semihemispherical droplet shape.

The difference in temperature between the vapor and the condensing surface can be expressed as

$$\Delta T = \Delta T_c + \Delta T_i + \Delta T_d + \Delta T_w \tag{29.4}$$

where ΔT is the total temperature difference $\left(T_i^g - T_o^w\right)$ (K); ΔT_c is the temperature drop due to droplet curvature (K); ΔT_i is the temperature drop at the vapor/liquid interface $\left(T_i^g - T_i^d\right)$ (K); ΔT_d is the temperature drop in the liquid layer $\left(T_i^d - T_i^w\right)$ (K); ΔT_w is the temperature drop in the promoter layer $\left(T_i^w - T_o^w\right)$ (K).

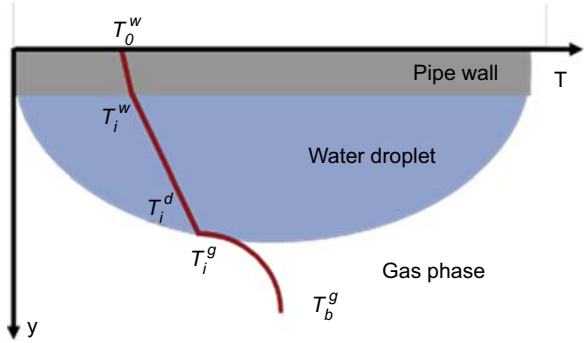

Figure 29.1 Description of the temperature gradient for a single droplet with T_o^w as the outer promoter temperature; T_i^w as the inner promoter temperature; T_i^d as the interfacial temperature in the liquid side; T_i^g as the interfacial temperature in the gas side; and T_b^g as the bulk gas temperature.
Adapted from Z. Zhang, D. Hinkson, M. Singer, H. Wang, S. Nesic, A mechanistic model for top of the line corrosion, Corrosion 63 (11) (November 2007) 1051−1062.

The temperature gradients are calculated the following way:

- Temperature drop due to droplet curvature [12]

$$\Delta T_c = \frac{2T_i^g \sigma}{H_{fg} r \rho_w} \tag{29.5}$$

where r is the radius of the droplet (m); σ is the vapor−liquid surface tension (N/m); ρ_w is the water density (kg/m^3).

- Temperature drop due to vapor/liquid interface [15]

$$\Delta T_i = \frac{q}{2\pi r^2 h_i} \tag{29.6}$$

where h_i is the heat transfer coefficient at the droplet interface (W/m^2/K).

- Temperature drop through the liquid droplet [16]

$$\Delta T_d = \frac{q \times r}{4\pi r^2 k_c} \tag{29.7}$$

where k_c is the water thermal conductivity (W/m/K).

- Temperature drop through the promoter layer [12]

$$\Delta T_w = \frac{q \times L_p}{4\pi r^2 k_p} \tag{29.8}$$

where k_p is the promoter thermal conductivity (W/m/K) and L_p is the thickness of the promoter layer (m).

Finally, the heat flux through a single droplet can be expressed by combining all of the equations given earlier:

$$q(r) = \frac{T_i^g\left(1 - \dfrac{2\sigma}{H_{fg} r \rho_w}\right) - T_o^w}{\dfrac{r}{4\pi r^2 k_c} + \dfrac{1}{2\pi r^2 h_i} + \dfrac{L_p}{4\pi r^2 k_p}} \tag{29.9}$$

where $q(r)$ is the heat flux through an individual droplet of radius r (W/m^2).

The expression of the dropsize distribution was developed by Le Fevre [17] and is commonly accepted by many authors [3,4,18,19] in the following form:

$$N(r)dr = \frac{1}{3 \times \pi \times r^2 \times r_{\max}} \times \left(\frac{r}{r_{\max}}\right)^{-\frac{2}{3}} dr \tag{29.10}$$

where $N(r)dr$ is the number of drops per area with radius between r and $r + dr$ (m^{-2}); r is the radius of the droplet (m); $r_{\max}$ is the maximum droplet radius (m).

The final equation becomes

$$h_g \times \left(T_b^g - T_i^g\right) + \mathrm{WCR} \times H_{fg} = \int_{r_{\min}}^{r_{\max}} \frac{T_i^g\left(1 - \dfrac{2\sigma}{H_{fg} r \rho_w}\right) - T_o^w}{\dfrac{r}{4\pi r^2 k_c} + \dfrac{1}{2\pi r^2 h_i} + \dfrac{L_p}{4\pi r^2 k_p}} \times \frac{1}{3\pi r^2 r_{\max}} \left(\frac{r}{r_{\max}}\right)^{-\frac{2}{3}} dr \tag{29.11}$$

The expression of the size of the smallest thermodynamically viable droplet is [11]

$$r_{\min} = \frac{2T_s\sigma}{H_{fg}\rho_w \Delta T} \tag{29.12}$$

where T_s is the aturation temperature (K).

The maximum droplet size based on a dimensional analysis is expressed as [4]

$$r_{\max} = K \times \left(\frac{\sigma}{\rho_w g}\right)^{0.5} \tag{29.13}$$

where K is the experimentally defined constant close to unity; g is the gravitational acceleration (m/s^2).

Eqs. (29.11) still contains two unknown variables, namely WCR and the interfacial temperature in the gas side T_i^g. Consequently, another equation is needed to solve the

problem. Zhang [10] added a mass balance of the water in order to calculate the condensation rate:

$$\mathrm{WCR} = \rho_g \beta_g \times \left(x_b^g - x_i^g\right) = \rho_g \beta_g \times \frac{M_w}{P_T M_g}\left(P_{\mathrm{sat}}\left(T_b^g\right) - P_{\mathrm{sat}}\left(T_i^g\right)\right) \qquad (29.14)$$

where WCR is given as kg/m^2/s; β_g is the mass transfer coefficient in the gas boundary layer (m/s); x_b^g is the mass fraction of water vapor in the bulk gas flow ($\mathrm{kg_v/kg_g}$); x_i^g is the mass fraction of water vapor at the gas-liquid interface ($\mathrm{kg_v/kg_g}$); ρ_g is the density of gas ($\mathrm{kg_g/m^3}$); M_w and M_g are the molecular weight of the water and the gas mixture (g/mol); P_T is the total pressure (Pa); P_{sat} is the saturation pressure as a function of temperature (Pa).

Zhang [10] was the first to propose a dropwise condensation approach to calculate the WCR in a TLC configuration. Since then, Pojtanabuntoeng [20,21] and, later, Gao [22] have upgraded this model to include the prediction of co-condensation of hydrocarbon and the effect of glycol on the overall condensation process, respectively.

As shown earlier, this approach calculates a local condensation rate at the 12 o'clock position of a pipeline. In contrast, the water dropout approach described in the previous section calculates an overall water accumulation rate considering the net effect between the vapor condensation and the water evaporation from the brine.

29.2 Review of existing TLC models

This section presents different attempts to model TLC and predict rates of corrosion considering either empirical and semiempirical or mechanistic approaches.

29.2.1 Empirical and semiempirical approaches

In 1991, Olsen [23] was the first to lay out the fundamental concepts of CO_2-dominated TLC modeling, which are still valid today and are at the core of most current TLC models. Olsen stated that the competition between corrosion (Fe^{2+} source) and condensation (Fe^{2+} source) controls the $FeCO_3$ saturation level and, consequently, the level of protectiveness of the corrosion product and the extent of the corrosion attack. At high temperatures $\geq$70°C (158°F) and low condensation rate, a dense and protective $FeCO_3$ is favored. At high condensation rate, the saturation in $FeCO_3$ is more difficult to obtain due to the rate of fresh water renewal. Although no proper mathematical model was proposed, this work is fundamental in many respects.

The first actual TLC prediction equation in sweet environments was proposed by DeWaard [24] who adapted his well-known correlation to a TLC scenario. DeWaard introduced a correcting factor $F_{\mathrm{Cond}} = 0.1$ in order to adapt his model to condensation conditions for condensation rates below an experimentally determined critical rate of 0.25 mL/m^2 s. This equation is still widely used today due to its simplicity but gives an

extremely conservative prediction. For instance, the presence and effect of $FeCO_3$ is completely ignored.

$$CR = F_{Cond} \times 10^{\left(5.8 - \frac{1710}{T_k} + 0.67 \times \log\left(p_{CO_2}\right)\right)} \tag{29.15}$$

where P_{CO_2} is the partial pressure of CO_2 (bar); T_k is the temperature (K); F_{Cond} is 0.1; CR is the corrosion rate (mm/year).

In 2000, Pots [25] proposed a more comprehensive attempt to mathematically represent the competition between the scale formation rate—linked to the iron dissolution—and the condensation rate. Pots developed the so-called "supersaturation model" based on the calculation of the concentration of iron at saturation under film-forming conditions. The corrosion rate CR, calculated using the formula below, is equated with the precipitation rate PR, calculated using an equation developed by Van Hunnik [26]. The concentration of Fe^{2+} present on both sides of the equations (Eqs. 29.16 and 29.17) is calculated and reinserted in the corrosion rate equation. This approach highlighted the need to develop in parallel a solid chemistry model as well as a correct evaluation of the condensation rate in order to accurately predict the corrosion rate. However, no clear guidelines on how to calculate it were provided.

$$CR = \frac{M_{Fe} \times 10^6 \times 24 \times 3600 \times 365}{\rho_{Carbonsteel}} \times \left[Fe^{2+}\right]_{supersat} \times \frac{WCR}{\rho_w} \tag{29.16}$$

where CR is the corrosion rate (mm/year); WCR is given as $g/m^2/s$; ρ_w is the water density (g/m^3); $[Fe^{2+}]_{supersat}$ is the iron concentration at $FeCO_3$ saturation (mol/L); M_{Fe} is the iron molecular weight (55.847 g/mol); $\rho_{carbonsteel}$ is the density of a typical carbon steel (CS) (7,860,000 g/m^3).

$$PR = A_p \times e^{\frac{-E_a}{RT}} \times K_{sp} \times (s-1)\left(1 - \frac{1}{s}\right) \text{ and } s = \frac{\left[Fe^{2+}\right] \times \left[CO_3{}^{2-}\right]}{K_{sp}} \tag{29.17}$$

where PR is the precipitation rate converted in $mol/m^2/s$; A_p is the constant E_a is the activation energy (KJ/mol); R is the deal gas constant (J/K/mol); T is the temperature (K); s is the $FeCO_3$ saturation; K_{sp} is the $FeCO_3$ solubility product (mol^2/m^2).

Based on the same concepts, Nyborg et al. [27] developed in 2007 a new empirical equation validated through experimental work. The expression developed by Nyborg depends on the WCR, the iron carbonate solubility and a supersaturation factor. According to the author, it is valid only for low acetic acid content (<0.001 mol/L), low to medium carbon dioxide partial pressure <3 bars (44 psi), and no H_2S. The iron carbonate solubility is represented as "solubility of iron ion" and is expressed as a function of temperature, total pressure, and CO_2 partial pressure. This calculation step requires a comprehensive water chemistry module, which can be adapted to include the effect of organic acid and glycol content [28]. Although no detail is provided on how the condensation rate is calculated, Nyborg stresses the importance of

predicting an accurate condensation rate, as it will have a much more pronounced effect on TLC than, for example, the CO_2 partial pressure.

$$\mathrm{CR} = 0.004 \times \mathrm{WCR} \times \left[\mathrm{Fe}^{2+}\right] \times (12.5 - 0.09 \times T) \tag{29.18}$$

where CR is the corrosion rate (mm/year); WCR is given as g/m^2/s; [Fe^{2+}] is the solubility of iron ions (ppm_w); T is the temperature (°C).

29.2.2 Mechanistic models

Mechanistic efforts to model TLC date back to early 2000 and focus exclusively on sweet (CO_2 dominated) environments. These mechanistic efforts usually yield vastly more accurate predictions but are much more cumbersome to implement as they typically require solutions to systems of nonlinear differential equations. Although much progress has been made in the understanding of sour TLC and sour corrosion in general, no modeling approach has been properly validated.

In 2002, Vitse [29–31] presented the first mechanistic attempt to model both condensation and corrosion processes. Vitse's condensation model assumed a continuous water film thickness mostly dependent on surface tension according to the following equation:

$$\delta = \left(\frac{\sigma}{g \times (\rho_l - \rho_g)}\right)^{0.5} \tag{29.19}$$

where g is the gravitational acceleration (m/s^2); σ is the surface tension (N/m); ρ_l and ρ_g are liquid and gas density, respectively (kg/m^3).

Considering the phase change and the heat resistance through the pipe wall and water layer, Vitse used Nusselt's theory of filmwise condensation [32,33] to develop his model. However, Vitse acknowledged that this approach was not properly suited to simulate the condensation process at the top of the line, which is dropwise [34]. Vitse then directly used the film-free electrochemical model proposed by Nesic [35] to estimate the corrosion rate. Furthermore, he conducted an Fe^{2+} flux balance in the droplet, taking into account the fluxes of Fe^{2+} created by corrosion, removed by $FeCO_3$ precipitation and transported by condensed water film convection. The $FeCO_3$ precipitation rate is calculated using the expression from Van Hunnik [26]. The role of the corrosion product layer was simplified by considering that the part of the steel surface covered by $FeCO_3$ was not corroding. The estimation of this covering factor K was done empirically, by fitting with experimental data. Under this model, an iterative process is performed until no change in the iron ion concentration is computed inside the control volume. Although still based on the fundamental mechanisms initially proposed by Olsen [23], and although not fully mechanistic, Vitse's method gave insight into how to model TLC phenomena. The equation used in the Fe^{2+} flux balance is displayed below:

$$\frac{d\left[\mathrm{Fe}^{2+}\right]}{dt} = \frac{1}{\delta} \times \left[K \times \mathrm{CR} - (1 - K) \times \mathrm{PR} - \mathrm{WCR} \times \left[\mathrm{Fe}^{2+}\right]\right] \tag{29.20}$$

where Fe^{2+} is the concentration of iron ion inside the control volume (mol/m^3); t is the time (s); CR is the corrosion rate (mol/m^3/s); PR is the precipitation rate (mol/m^3/s); WCR is given as m^3/m^2/s; δ is the liquid film thickness (m); K is the covering factor.

In 2007, Zhang et al. [10] published the first fully mechanistic approach to TLC modeling. Like Vitse's approach [29−31], the model covers the three main processes involved in top of the line corrosion (TLC) phenomena: dropwise condensation, chemistry in the condensed water, and corrosion at the steel surface. The condensation model, based on a dropwise approach valid for the 11−1 o'clock position in a pipeline, is presented in the previous section. The chemistry of the condensed liquid is established through standard chemical and thermodynamic equations [36,37]. Finally, the corrosion model is directly adapted from the mechanistic CO_2 corrosion approach developed by Nordsveen et al. [38] and Nesic et al. [39,40]. This corrosion model considers chemical reactions, transport of species, and the electrochemical reactions at the metal surface. For instance, the expression of the transport of chemical species in the liquid film and the porous corrosion product can be simplified assuming no convection (stagnant droplet):

$$\frac{\partial \varepsilon C_i}{\partial t} = D_i \frac{\partial^2 (\kappa C_i)}{\partial x^2} + \varepsilon R_i \tag{29.21}$$

where C_i is the concentration of species i (mol/L); ε is the volumetric porosity of the film, equal to 1 outside the corrosion product layer; κ is the surface permeability of the film, equal to 1 outside the corrosion product layer; D_i is the molecular diffusion of species i (m^2/s); R_i is the source or sink of species i (mol/L/s); t is the time (s); x is the spatial coordinate (m).

The porosity ε can be expressed as a function of the $FeCO_3$ precipitation rate, defined by the Van Hunnik equation [26] for $FeCO_3$ dissolution/precipitation rate:

$$\frac{\partial \varepsilon}{\partial t} = -\frac{M_{FeCO_3}}{\rho_{FeCO_3}} R_{FeCO_3} \tag{29.22}$$

where M_{FeCO_3} is the iron carbonate molecular weight (kg/mol); ρ_{FeCO_3} is the iron carbonate density (k/m^3); R_{FeCO_3} is the iron carbonate precipitation rate (mol/m^3/s).

The flux of electroactive species is calculated with the following equation:

$$N_j = -\frac{i_j}{n_j F} \tag{29.23}$$

where i_j is the current density for species j (A/m^2); n_j is the number of electrons exchanged for species j; F is the faraday number (A·s/mol); N_i is the flux of species j (mol/m^2/s).

Finally, the current density of each corrosive species can be expressed following the Tafel approximation:

$$i = \pm i_0 \cdot 10^{\pm \frac{E - E_{rev}}{b}} \tag{29.24}$$

where i_0 is the exchange current density; E_{rev} is the reversible potential; b is the tafel slope.

This system constitutes a set of nonlinear differential equations that need to be solved both in time and space. Zhang's innovation is to adapt these models to a TLC scenario. Zhang's main assumption is that the steel surface is corroding uniformly considering that, although the condensation is dropwise, every point on the metal surface has the same probability of being covered by liquid droplets. The problem can then be simplified from a three-dimensional (semihemispherical droplet) to a one-dimensional (1-D; liquid layer) problem. The validity of this 1-D assumption with respect to the occurrence of localized corrosion is discussed later in this chapter. The droplet growth is simulated by considering the increase in liquid film thickness due to the condensation process. Once the droplet reaches a calculated maximum size, the liquid film thickness is reset to its initial value, simulating a situation where the droplet either slides or falls due to gravity forces. This cycle is carried out until the corrosion process reaches a steady state. Fig. 29.2 shows how the calculation domain is structured and how the boundary conditions, at the steel surface and the liquid vapor interface, are defined.

This approach represents to date the most comprehensive attempt to model TLC as it takes into account all of the controlling parameters following a fully mechanistic methodology.

In 2011, Asher presented a comprehensive summary on best modeling practices related to sweet and sour TLC [42]. Although no specific algorithm was presented in the publication, the approach seemed to agree with Zhang's methodology, stressing the importance of the chemical, condensation, and corrosion processes and highlighting the balance between the fluxes of iron ions due to corrosion and required to form the corrosion product layer.

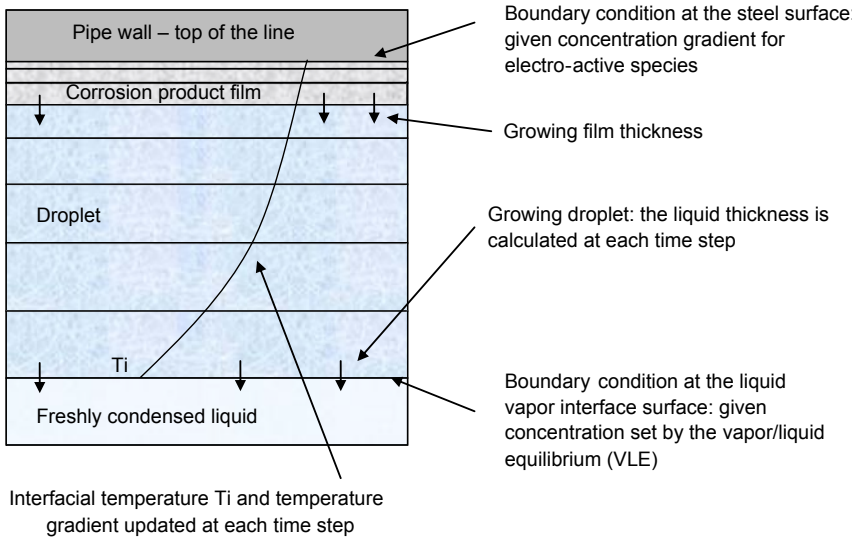

Figure 29.2 Schematic of the corrosion calculations in a growing droplet [41].

29.2.3 Prediction of localized corrosion

As mentioned in Chapter 16, sweet TLC is thought to be a "uniform" localized corrosion phenomenon instead of a purely pitting-dominated process. The "uniform" qualification of the attack is supported by the large size of the features and the extent of the corrosion rate, which never surpasses the "layer-free" rate. It is thought that the penetration rate is driven by the corrosivity of the environment and the WCR and is not particularly affected by any galvanic coupling between bare steel and layer-covered areas of the steel surface.

However, understanding and modeling how the localized corrosion features initiate, grow, and eventually coalescence in a dewing environment is of great importance. As for any type of localized corrosion in a sweet environment, a prerequisite of any local attack is a formation of a partially protective $FeCO_3$ scale. Based on an experimental study performed at the bottom of the line, Sun was able to identify a zone where localized corrosion occurrence and propagation were most likely [43]. The presence of a partially protective $FeCO_3$ was crucial, as under film-free or fully protective film conditions, no localized corrosion was observed. The scaling tendency (i.e., the ratio of precipitation and corrosion rate) was introduced to quantify the likelihood of localized corrosion occurrence. The precipitation rate was directly derived for the $FeCO_3$ saturation level in the bulk phase, which could also be used to evaluate the protectiveness of the scale.

The possibility of a galvanic affect between the bottom of the mesa attack feature (film-free) and the surrounding area covered with $FeCO_3$ was also introduced by Han [44–47]. The induced difference in potential could accelerate the corrosion rate of the exposed steel. Using a novel experimental setup artificially simulating a pit, Han could actually measure the difference in potential between the film-covered surface and the film-free site of the bottom of the pit. He could also link the localized corrosion growth with a $FeCO_3$ saturation level between 0.5 and 2, as did Sun et al. [43]. More importantly, Han stipulated that the pH of the solution trapped between the corrosion product layer and the steel was actually much higher than the pH in the bulk, leading to the formation of thin iron oxide (Fe_3O_4) film. This layer could provide an explanation for the significant increase in potential of the film-covered "passive" surface and the establishment of a galvanic cell with the active site of the pit. However, the existence of the iron oxide film has been debated as attempts by several authors to identify the oxide layer were inconclusive at best [46,48]. In addition, the mechanism cannot be applied easily to a dewing environment because the condensed water is not sufficiently conductive to "carry" the current at any significant level.

In 2008, Amri [49,50] performed similar experiments in an effort to relate pit growth and environmental conditions, especially in the presence of acetic acid. It was found that the growth of the pit was related to the depletion of the acetic acid concentration inside the pit. It was also stated that the growth should stop once the pit reaches a certain depth. Many of the observations made by the author were typical of a TLC scenario and were put forward to explain TLC stabilization. Consequently, this study constituted the first attempt to adapt the localized corrosion process to TLC.

Later, in 2013, Singer performed a comprehensive experimental study focused on the localized nature of TLC in sweet environments [41]. The author clearly identified

conditions where little to no corrosion was observed (low WCR and CO_2 content), where localized corrosion was present (moderate condensation rate, high gas temperature, and high organic acid content), and where uniform corrosion dominated (low steel temperature and high WCR). From these observations, the author developed a narrative for localized corrosion initiation and growth:

1. Initially, the steel surface corrodes uniformly and the rate of corrosion decreases with time due to the increase in solution pH (Fe^{2+} ions accumulation inside the droplet). The situation lasts as long as the droplet remains undersaturated with respect to $FeCO_3$.
2. If the $FeCO_3$ saturation level reaches one, the formation of the corrosion product layer decreases the corrosion rate even further. (Practical laboratory experience shows that supersaturation values of 5−10 are often sustainable, especially at high temperature [51].)
3. The condensation rate of fresh water being constant, the droplet eventually becomes slightly undersaturated, leading part of the layer to redissolve. The steel surface can become segregated between areas well-protected by the $FeCO_3$ layer and uncovered areas suffering from "bare steel" corrosion.
4. Uncovered areas corrode actively, whereas covered areas are protected, but the overall flux of Fe^{2+} ions due to corrosion, averaged over the entire steel surface, becomes constant in order to maintain the $FeCO_3$ saturation level. Localized TLC features are created.
5. The localized features initially propagate in depth as the immediate surroundings are covered by protective $FeCO_3$. However, the corrosion also progresses laterally, underneath the already existing $FeCO_3$ layer. The deeper features may stop progressing in depth while new damages in the corrosion product layer appear.

This narrative explains why the overall wall thickness loss rate becomes constant while localized features are present. The overall rate of iron dissolution is controlled by the corrosivity of the droplet, considering the chemistry at $FeCO_3$ saturation.

29.3 Remaining gaps in the modeling of TLC mechanisms

29.3.1 Prediction of sour TLC

Although much progress has been achieved in sweet TLC prediction, the modeling of sour corrosion remains a considerable challenge. As mentioned in Chapter 16, sour TLC is much less dependent on the WCR and seems to be controlled by the properties of the corrosion product layer. Most of the more mechanistic models have been adapted to predict sour TLC, a task made possible due to their fundamental physical structure [52]. However, comprehensive validation of these models has been difficult due to the lack of accurate field data. Occurrence of sour TLC is rare and often difficult to clearly identify. In addition, modeling of sour TLC clearly lags behind modeling of sour corrosion, and proper understanding of the effect of Fe_xS_y corrosion product layers on corrosion and pitting is lacking.

29.3.2 Modeling of TLC stabilization

Modeling approaches based on a uniform corrosion mechanism have been successfully used to predict the trend and order of magnitude of TLC, at least in sweet

environments. By itself, this observation represents a validation of this choice of overall mechanism. However, it also means that, for a fixed set of operating conditions, wall loss due to TLC is expected to occur continuously over the production life. As mentioned in Chapter 16, in-line inspections (ILIs) have shown that TLC features stop progressing in depth after some time, a phenomenon called TLC stabilization [53]. Current models cannot explain this behavior completely: although individual TLC features may very well cease to progress in depth due to geometrical considerations and mass transfer limitations, it is expected that other nearby features should "take over" or new features should appear in order to maintain the overall Fe^{2+} flux and the $FeCO_3$ saturation. Field evidence of TLC stabilization is still controversial and the phenomenon has not been comprehensively investigated in a laboratory. Consequently, the lack of widely approved explanation for TLC stabilization makes its modeling quite challenging for now.

29.3.3 Limitations in the use of TLC predictive models

Using corrosion models that have been developed in academic and research institutions and applying them to field conditions has always been a challenge. On one hand, researchers are often hesitant to use incomplete and inaccurate field data to validate their models. On the other hand, field engineers often distrust the models' ability to simulate complex field conditions, preferring to rely exclusively on field experience, as the models' validity and limitations are often misunderstood. Comprehensive and open validation of modeling performances with field experiences involving actual pipeline TLC failures is an essential step in bridging that gap. The first comprehensive effort to compare modeling predictions with TLC field data was performed by Gunaltun in 2010 [54]. The author selected 11 flow lines and determined a set of average operating conditions (temperature, pressure, CO_2 content, and flow rates) for each of them. These data were fed as input parameters for the TLC model, which was based on Zhang's approach [10]. One single TLC rate was predicted for each flow line and compared to maximum thickness loss measurements obtained through magnetic flux leakage (MFL) inspection. The comparison between the predicted TLC rates and the maximum measurable thickness losses showed a generally poor degree of agreement.

However, this effort was successful in highlighting some of the difficulties related to the development an accurate methodology for comparing model and field data. Among them, averaging decades of fluctuating operating conditions into one single set of parameters cannot be seen as an accurate representation of the production history. In addition, taking the maximum thickness loss measured from an MFL run cannot be used to represent the overall severity of the corrosion attack along a given pipeline. Too much confidence is often placed in ILI data, and the inaccuracy of the inspection tools must be accounted for, especially when comparing successive runs. In summary, efforts must be made both to ensure that the models are fed with the most accurate conditions possible and that the ILI data extracted for comparison are indeed representative of the TLC severity.

29.4 Best practices and emerging trends

As described earlier, comparison between model predictions and field data is still a difficult exercise. Often, the models are quickly blamed for their perceived ineffectiveness while too much trust is placed on notoriously inaccurate field data. In any case, the quality of the model predictions cannot be expected to be of better than the input field data.

29.4.1 Methodology for comparing field data and model prediction

In 2012, Kaewpradap developed a comprehensive methodology aimed at effectively utilizing both field data and model predictions [55–57]. The author identified several challenges and separated them into three main groups.

29.4.1.1 Issues related to the accuracy of field data

Kaewpradap listed all the field parameters needed to perform a proper simulation: history of production data, inlet pressure and temperature, gas and liquid composition. The author also highlighted the importance of topographic data, burial depth, environmental conditions, and pipeline properties. Some of these parameters can vary greatly over the course of a field's production life. Mechanistic models are very sensitive to this information, both for the calculation of the WCR and the TLC rate. As much as possible, the collection of complete and accurate field data is a definite prerequisite.

29.4.1.2 Issues related to the model predictions

The author highlighted the importance of fully understanding the meaning of predicted parameters. Most current models calculate steady-state uniform corrosion rates. The validity of using uniform corrosion models to simulate localized TLC features has been debated earlier in this section. Based on the current understanding of the mechanism, predicted steady-state corrosion rates apply to the growth of large mesa-type corrosion features but not pitting. It is also clear that current TLC models cannot be used to simulate corrosion rates at the bottom of the line, or defects at field joints, for example. Simulated corrosion rates are only valid for one set of input conditions, and calculations need to be repeated and integrated over time in order to represent the total wall thickness loss experienced over an entire production history. It is often necessary to identify production periods showing similarities and determine time-averaged input parameters over several time periods in order to balance practicality and accuracy.

29.4.1.3 Issues related to the analysis of ILI data

It is crucial to understand how the TLC feature size is actually measured, whether the ILI is performed through MFL, ultrasonic testing, or any other nondestructive testing tool. For instance, MFL, which is the most widely used technique, determines the

feature depth by converting deviation in magnetic flux using proprietary algorithms. In addition, typical accuracy is on the order of 10%−20% of the nominal wall thickness [58]. ILI data logs contain a wealth of information, most of it not directly related to TLC. These data must be filtered in order to identify large features (clusters not pitting) located at the 10−2 o'clock position and to eliminate noisy data related to field joint or girth welds.

Based on these observations, Kaewpradap proposed a multistep methodology for the comparison of model predictions and field data, considering a given pipeline [57].

Field condition analysis

Step 1: Identification of operating time periods showing similarities in term of inlet temperature and pressure, gas−liquid flow rates, and determination of a simple, time-averaged value for each operating parameter
Step 2: Calculation of WCRs and temperature profiles using a heat and mass transfer line model
Step 3: Simulations of steady-state TLC rate along the pipeline for each time period
Step 4: Calculation of cumulative wall thickness losses for the entire operating life of the field and comparison with provided MFL data

ILI data analysis

Step 1: Selection of ILI data over sections of pipe where the most severe TLC is typically encountered (start of line except riser, cold spots)
Step 2: Omission of features in the section of line where flow regime is clearly not stratified (vertical riser)
Step 3: Selection of features in the upper section of the pipe (between 10 and 2 o'clock)
Step 4: Omission of features located ±0.5 m around the weld joints
Step 6: Selection of large clusters and omission of small-size, isolated features. (Clusters are defined as large corrosion features, where width and depth is at least three times the wall thickness, following the classifications developed by the pipeline operators forum [59]).

Kaewpradap implemented this procedure to simulate several fields in the gulf of Thailand and obtained reasonably good agreement with field data [55,57]. Some discrepancies remain, as expected, especially in the prediction of the severity of the TLC attack in the first hundreds meters of line. The model, following the author's current understanding of the mechanisms, predicts the highest TLC rate at the inlet of the pipe, whereas ILI data show that the wall thickness loss typically reaches its maximum only after a few 100 m. The reason behind this behavior is not understood and requires further investigation.

29.4.2 How to use TLC prediction?

There is no question that corrosion prediction models in general should always be used in conjunction with field experience. This is also true for TLC prediction models. Recent efforts use some of these models to explain measured high thickness losses have been successful, validating this use of the tool for failure analysis.

TLC prediction software can also be used for the design of new pipelines. Examples are as follows:

- The expected operating conditions and production flow rates can be used to evaluate the TLC severity and implement the appropriate design decisions: corrosion allowance, characteristics of thickness of thermal insulation [53,60].
- Corrosion resistant alloy (CRA) and cladded pipe have been used for cooling spool pieces, where the vapor is forced to condense with no risk for the pipe material. TLC models can be used to determine the optimal length of the CRA spool piece [53].
- The transition between CRA and CS sections can also pose an elevated risk of corrosion as fresh condensed water, containing no dissolved iron ions, can travel to the CS section [53]. Although this does not constitute a pure case of TLC, existing models can be used to predict the severity of the corrosion attack. Similarly, the expected TLC rates at tie-ins can also be evaluated in a similar way.
- Expected TLC rates can be used to prioritize ILI runs on lines that are found more critical [60].
- The frequency of batch inhibition can be determined using predicted TLC rates [60], although the inhibition persistency is also a required parameter that can only be obtained through field experience or laboratory evaluation.

29.5 Conclusions

Much progress has been made over the past 20 years with regards to the understanding and modeling of TLC. Academic and research institutions have conducted carefully designed experimental studies and developed models that can accurately simulate this corrosion phenomenon. Efforts are still needed to fully represent the complexity of field environments, but TLC prediction software has been used with growing confidence by the industry, partly due to comprehensive and open validation activities.

References

[1] P. Meakin, Dropwise condensation: the droplet growth and coalescence of fluid droplets, Physica Scripta T44 (Febuary 1992) 31–41.
[2] J.W. Rose, On the mechanism of dropwise condensation, International Journal of Heat and Mass Transfer 10 (1967) 755–762.
[3] J.W. Rose, Dropwise condensation theory and experiment: a review, Journal of Power and Energy 216 (2002) 115–128.
[4] J.W. Rose, Dropwise condensation theory, International Journal of Heat and Mass Transfer 24 (1981) 191–194.
[5] J.W. Rose, On interphase matter transfer, the condensation coefficient and dropwise condensation, Proceedings of the Royal Society of London, Series A, Mathematical and Physical Sciences 411 (1841) (June 1987) 305–311.
[6] J.W. Rose, Some aspects of condensation heat transfer theory, International Communication in Heat and Mass Transfer 15 (1988) 449–473.

[7] D.W. Tanner, C.J. Potter, D. Pope, D. West, Heat transfer in dropwise condensation − Part1 & 2, International Journal of Heat and Mass Transfer 8 (1965) 419−426, 426−436.
[8] C.Y. Wang, C.J. Tu, Effect of non-condensable gas on laminar film condensation in a vertical tube, International Journal of Heat and Mass Transfer 31 (11) (1988) 2339−2345.
[9] S. Wang, Y. Utaka, Effect of non-condensable gas mass fraction on condensation heat transfer for water-ethanol vapor mixture, JSME International Journal, Series B 47 (2) (2004) 162−167.
[10] Z. Zhang, D. Hinkson, M. Singer, H. Wang, S. Nesic, A mechanistic model for top of the line corrosion, Corrosion 63 (11) (November 2007) 1051−1062.
[11] C. Graham, P. Griffith, Drop size distribution and heat transfer in dropwise condensation, International Journal of Heat and Mass Transfer 16 (1973) 337−346.
[12] M. Abu-Orabi, Modeling of heat transfer in dropwise condensation, International Journal of Heat and Mass Transfer 41 (1998) 81−87.
[13] B.M. Burnside, H.A. Hadi, Digital computer simulation of dropwise condensation from equilibrium droplet to detectable size, International Journal of Heat and Mass Transfer 42 (1999) 3137−3146.
[14] S. Verumi, K.J. Kim, An experimental and theoretical study on the concept of dropwise condensation, International Journal of Heat and Mass Transfer 49 (2006) 649−657.
[15] J.R. Maa, Drop size distribution and heat flux of dropwise condensation, The Chemical Engineering Journal 16 (1978) 171−176.
[16] N. Fatica, D.L. Katz, Dropwise condensation, Chemical Engineering Progress 45 (11) (1949) 661−674.
[17] E.J. Le Fevre, J.W. Rose, A theory of heat transfer by dropwise condensation, Proceedings of Third International Heat Transfer Conference AIChE 2 (1966) 362.
[18] J.W. Rose, L.R. Glicksman, Dropwise condensation − the distribution of drop sizes, International Journal of Heat and Mass Transfer 16 (1973) 411−425.
[19] Y.T. Wu, C.X. Yang, X.G. Yuan, Drop distribution and numerical simulation of dropwise condensation heat transfer, International Journal of Heat and Mass Transfer 44 (2001) 4455−4464.
[20] T. Pojtanabuntoeng, M. Singer, S. Nesic, Water/hydrocarbon co-condensation and the influence on top-of-the-line corrosion, in: Proc. Corrosion, Houston, TX, 2011, Paper. 11330, 2011.
[21] T. Pojtanabuntoeng, M. Singer, S. Nesic, Top-of-the-line corrosion in the presence of hydrocarbon co-condensation in flowing condition, in: Proc. Corrosion, New Orleans, LA, 2012, Paper 1534, 2012.
[22] S. Guo, F. Farelas, M. Singer, Effect of monoethylene glycol on sweet top of the line corrosion, in: Proc. Corrosion, Vancouver, CA, 2016, Paper 7891, 2016.
[23] S. Olsen, A. Dugstad, Corrosion under dewing conditions, in: Proc. Corrosion, Houston, TX, 1991, Paper. 472, 1991.
[24] C. DeWaard, U. Lotz, D.E. Milliams, Predictive model for CO_2 corrosion engineering in wet natural wet gas pipelines, Corrosion 47 (12) (1991) 976−985.
[25] B.F.M. Pots, E.L.J.A. Hendriksen, CO_2 corrosion under scaling conditions − the special case of top-of-the-line corrosion in wet gas pipelines, in: Proc. Corrosion, Houston, TX, 2000, Paper. 31, 2000.
[26] E.W.J. Van Hunnik, B.F.M. Pots, E.L.J.A. Hendriksen, The formation of protective $FeCO_3$ corrosion product layers in CO_2 corrosion, in: Proc. Corrosion, Houston, TX, 1996, Paper. 6, 1996.
[27] R. Nyborg, A. Dugstad, Top of the line corrosion and water condensation rates in wet gas pipelines, in: Proc. Corrosion, Nashville, TN, 2007, Paper. 7555, 2007.

[28] G. Svenningsen, R. Nyborg, Modeling of Top of the line corrosion with organic acid and glycol, in: Proc. Corrosion, San Antonio, TX, 2014, Paper. 4057, 2014.
[29] F. Vitse, Y. Gunaltun, D. Larrey de Torreben, P. Duchet-Suchaux, Mechanistic model for the prediction of top-of-the-line corrosion risk, in: Proc. Corrosion, Houston, TX, 2003, Paper. 3633, 2003.
[30] F. Vitse, K. Alam, Y. Gunaltun, D. Larrey de Torreben, P. Duchet-Suchaux, Semi-empirical model for prediction of the top-of-the-line corrosion risk, in: Proc. Corrosion, Houston, TX, 2002, Paper. 2245, 2002.
[31] F. Vitse, Experimental and Theoretical Study of the Phenomena of Corrosion by Carbon Dioxide Under Dewing Conditions at the Top of a Horizontal Pipeline in Presence of a Non-condensable Gas (Ph.D. dissertation), Russ College of Eng., Dept. of Chem. Eng., Ohio Univ., Athens, OH, 2002.
[32] W. Nusselt, Die oberflächenkondensation des wasserdampfes, Zeitschrift des Vereines Deutscher Ingenieure 60 (27) (1916) 541−546.
[33] W. Nusselt, Die oberflächenkondensation des wasserdampfes, Zeitschrift des Vereines Deutscher Ingenieure 60 (28) (1916) 569−575.
[34] Y. Gunaltun, D. Larrey, Correlation of cases of top of the line corrosion with calculated water condensation rates, in: Proc. Corrosion, Houston, TX, 2000, Paper. 71, 2000.
[35] S. Nesic, J. Postlethwaite, S. Olsen, An electrochemical model for prediction of corrosion of mild steel in aqueous carbon dioxide solutions, Corrosion 52 (4) (1996) 280−294.
[36] D. Hinkson, M. Singer, Z. Zhang, S. Nesic, A study of the chemical composition and corrosiveness of the condensate in top of the line corrosion, in: Proc. Corrosion, New Orleans, LA, 2008, Paper. 8466, 2008.
[37] D. Hinkson, Z. Zhang, M. Singer, S. Nesic, Chemical composition and corrosiveness of the condensate in top-of-the-line corrosion, Corrosion 66 (4) (April 2010) 045001−045001-8.
[38] N. Nordsveen, S. Nesic, R. Nyborg, A. Stangeland, A mechanistic model for carbon dioxide corrosion of mild steel in the presence of protective iron carbonate films − Part 1: theory and verification, Corrosion 59 (5) (2003) 443−456.
[39] S. Nesic, N. Nordsveen, R. Nyborg, A. Stangeland, A mechanistic model for carbon dioxide corrosion of mild steel in the presence of protective iron carbonate films − Part 2: a numerical experiment, Corrosion 59 (6) (2003) 489−497.
[40] S. Nesic, N. Nordsveen, R. Nyborg, A. Stangeland, A mechanistic model for carbon dioxide corrosion of mild steel in the presence of protective iron carbonate films − Part 3: film growth model, Corrosion 59 (7) (2003) 616−628.
[41] M. Singer, Study and Modeling of the Localized Nature of Top of the Line Corrosion (Ph.D. dissertation), Russ College of Eng., Dept. of Chem. Eng., Ohio Univ., Athens, OH, 2013.
[42] S.L. Asher, W. Sun, R.A. Ojifinni, S. Ling, C. Li, J.L. Pacheco, J.L. Nelson, Top of the line corrosion modeling in wet gas pipelines, in: Proc. 18th International Corrosion Congress, Perth, Australia, 2011, Paper. 303, 2011.
[43] Y. Sun, S. Nesic, A parametric study and modeling on localized CO_2 corrosion in horizontal wet gas flow, in: Proc. Corrosion, Houston, TX, 2004, Paper. 4380, 2001.
[44] J. Han, Y. Yang, B. Brown, S. Nesic, Electrochemical investigation of localized CO_2 corrosion on mild steel, in: Proc. Corrosion, Nashville, TN, 2007, Paper. 7323, 2007.
[45] J. Han, Y. Yang, S. Nesic, B. Brown, Role of passivation and galvanic effects in localized CO_2 corrosion of mild steel, in: Proc. Corrosion, New Orleans, LA, 2008, Paper. 8332, 2008.
[46] J. Han, Galvanic Mechanism of Localized Corrosion for Mild Steel in Carbon Dioxide Environments (Ph.D. dissertation), Russ College of Eng., Dept. of Chem. Eng., Ohio Univ., Athens, OH, 2009.

[47] J. Han, D. Young, H. Colijn, A. Tripathi, S. Nesic, Chemistry and structure of the passive film on mild steel in CO_2 corrosion environments, Industrial and Engineering Chemistry Research 48 (2009) 6296−6302.
[48] W. Li, Investigation of Pseudo-Passive Layer Formation in CO_2 Corrosion (Master's thesis), Russ College of Eng., Dept. of Chem. Eng., Ohio Univ., Athens, OH, 2011.
[49] J. Amri, E. Gulbrandsen, R.P. Nogueira, The effect of acetic acid on the pit propagation in CO_2 corrosion of carbon steel, Electrochemistry Communications, 10 (2008) 200−203.
[50] J. Amri, E. Gulbrandsen, R.P. Nogueira, Propagation and arrest of localized attacks in carbon dioxide corrosion of carbon steel in the presence of acetic acid, Corrosion 66 (3) (March 2010) 035001−035001-7.
[51] Y. Yang, Removal Mechanisms of Protective Iron Carbonate Layer in Flowing Solutions (Ph.D. dissertation), Russ College of Eng., Dept. of Chem. Eng., Ohio Univ., Athens, OH, 2012.
[52] M. Joosten, D. Owens, A. Hobbins, H. Sun, M. Achour, D. Lanktree, Top-of-line corrosion − a field failure, in: Proc. EuroCorr, Moscow, Russia, 2010, Paper. 9524, 2010.
[53] Y. Gunaltun, Design of multiphase offshore pipelines with high risk of sweet top of the line corrosion, in: Proc. Corrosion, Orlando, FL, 2013, Paper 2290, 2013.
[54] Y. Gunaltun, M. Thammachart, M. Singer, S. Nesic, S. Punpruk, U. Kaewpradap, Progress in the prediction of top of the line corrosion and challenges to predict corrosion rates measured in gas pipeline, in: Proc. Corrosion, San Antonio, TX, 2010, Paper. 10093, 2010.
[55] U. Kaewpradap, M. Singer, S. Nesic, Top of the line corrosion − comparison of model predictions with field data, in: Proc. Corrosion, Salt Lake City, UT, 2012, Paper. 1449, 2012.
[56] U. Kaewpradap, Validation of Top of the Line Corrosion Prediction Model Using Laboratory and Field Measurements (Master's thesis), Ohio University, Chemical and Bio-molecular Engineering Department, 2012.
[57] U. Kaewpradap, M. Singer, S. Nesic, S. Punpruk, Comparison of model predictions and field data − the case of top of the line corrosion, in: Proc. Corrosion, Dallas, TX, 2015, Paper. 5809, 2015.
[58] R. Hall, M. McMahon, Report on the Use of In-Line Inspection Tools for the Assessment of Pipeline Integrity, US Department of Transportation, 2002. Report No. DTRS56-96-C-0002-008.
[59] Pipeline Operators Forum (POF) document, Specifications and Requirements for Intelligent Pig Inspection of Pipelines, 2009.
[60] M. Thammachart, Corrosion mitigation for pipeline failure due to top of the line corrosion, in: Proc. 3rd TOL Corrosion Conference, Bangkok, 2012, 2012.